Directing acoustic energy by flasher-based origami inspired arrays

Vivek Srinivas and Ryan L. Harne[a)]

Department of Mechanical and Aerospace Engineering, The Ohio State University, Columbus, Ohio 43210, USA

ABSTRACT:

Acoustic arrays with fixed spatial positions of transducers are used for wave guiding capabilities in the far field. Recent developments in the field of reconfigurable structures reveal that origami inspired foldable arrays may enhance the near and far field wave guiding functionality by virtue of physical shape change. This research explores reconfigurable acoustic arrays based on the deployable flasher tessellation frame using acoustic transducers at mountain crease nodes. Leveraging an experimentally validated model of the flasher acoustic array, this research reveals that arrays with transducers distributed about a spiral arm exhibit higher-order interference that results in broadside directive beam patterns at lower frequencies than radial arm distributions. The class of flasher arrays also exhibits a switching behavior from broadside directive to omnidirectional by virtue of distinct repositioning of the acoustic transducers in the folding process. The discoveries from this research motivate the use of flasher arrays for potential implementation in underwater applications. © 2020 Acoustical Society of America.
https://doi.org/10.1121/10.0002483

I. INTRODUCTION

To localize acoustic signals and map environments, arrays of acoustic transducer elements are distributed in distinct spatial arrangements. Phase delays and amplitude adjustments are often applied to transducer signals to adjust the operational capabilities of the arrays. The latter efforts constitute digital signal processing (DSP) that relies on knowledge of the transducer physical positioning to realize optimum array function.[1] DSP techniques for acoustic wave guiding have significantly evolved in recent decades, yet there remain intrinsic drawbacks. These include the computational expense to operate with real-time adaptation of function, questions of stability for real-time control, and limited portability due to the size and bulk of array implementations respecting frequency bands of interest.[2–4] Adaptive or "reconfigurable" DSP methods have been developed to capitalize on array transducer configurations known *a priori* that may change in space, number (e.g., due to transducer failure), or change due to electro-motive coupling (e.g., due to transducer damage).[5–8]

Yet, arrays utilizing uniform spacing of transducer elements, whether linear or planar, suffer from the intrinsic drawback of spatial aliasing that limits the frequency range of operation.[1] Consequently, non-uniformly spaced and randomly distributed array transducers are used to mitigate spatial aliasing and suppress grating lobes.[9–12] Moreover, it has been found that transducer element spacing should be irregular, or non-redundant, to suppress sidelobes from predominating beam patterns of microphone and hydrophone arrays.[13,14] The concept to devise acoustic array transducer

element spacing on the basis of spiral geometries has been broadly adopted to provide irregular element positioning that inhibits sidelobes, grating lobes, and spacing aliasing.[15] As a result, spiral arrays have received considerable attention as prospects for effective sound source localization and acoustic imaging.[16,17]

Providing new functionality to acoustic arrays necessitates a mechanism to augment intelligent array design and DSP foundations. In this report, physical array reconfiguration is considered as a means to enhance portability and surmount the fundamental frequency and spatial mapping capabilities of fixed array structures. Recently, reconfigurable structures inspired by origami[18] are being harnessed for a variety of adaptive acoustics applications, including for wave guides,[19–21] ultrasound transmitter arrays,[22,23] noise reduction,[24] wave filtering,[25,26] and sound absorbers.[27] The shapes of surfaces from which waves are transmitted or upon which waves are incident are central to the acoustic wave propagation behaviors. As a result, change of the shape leads to control over acoustic properties and therefore functionality. Here, the opportunity to tailor the beam patterns of microphone or hydrophone arrays is investigated using a reconfigurable structure platform that is distinctly effective for such purpose.

The "flasher" origami pattern is a rotationally symmetric set of creases that folds into a polygonal cylinder in the most compact state yet begins as an unfolded sheet.[28] The flasher has received considerable scientific attention for sake of deployable space structures,[29] medical devices,[30] and other packable structures with rotational symmetry.[31] An example of a flasher is given in Fig. 1(a). A non-dimensional flasher crease pattern is defined by three parameters: number of sectors m, number of rings r, and number

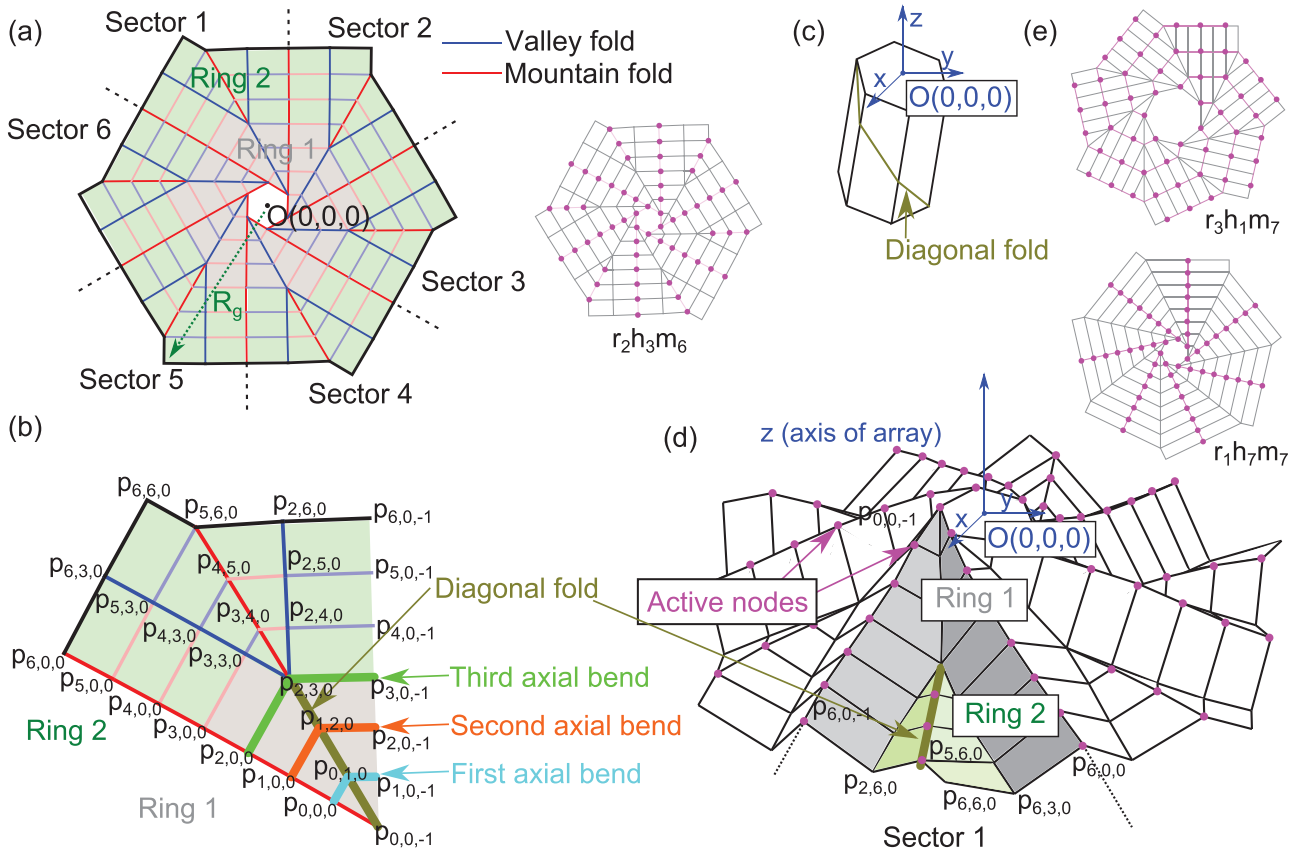a)Electronic mail: harne.3@osu.edu, ORCID: 0000-0003-3124-9258.

FIG. 1. (Color online) (a) 0% folded (unfolded) flasher array $r_2h_3m_6$ showing the crease pattern that is divided into six sectors. The inset illustrates the mountain nodes in magenta that are considered to have acoustic transducers. (b) Detailed representation of sector 1 from (a). (c) 100% folded (fully folded) flasher array as polygonal cylinder. Position of one of the diagonal folds in (b) is also shown. (d) 45% folded (partially folded) flasher array folding around z-axis. Nodes on mountain fold arm are active nodes marked as magenta circles. (e) 0% folded (unfolded) flasher arrays $r_3h_1m_7$ and $r_1h_7m_7$ showing the activated mountain nodes with magenta circles.

of axial bends on the diagonal of each ring h. For example, the flasher pattern in Fig. 1(a) is referred to as $r_2h_3m_6$, denoting the six sectors or edges of the central polygon, two rings in the radial direction, and the three axial bends on the ring diagonals. An unfolded flasher array is planar as seen in Fig. 1(a), which folds around the axis of array defined in Fig. 1(d). The flasher origami crease pattern is studied here due to the capability to fold into a compact polygonal cylinder and deploy it into a rotationally symmetric planar structure, observed comparing Figs. 1(c) and 1(d). The large kinematic reconfiguration is moreover reversible. The unfolded and folded radii may be used as design parameters to achieve target shape transformations for deployable system applications, such as underwater towed arrays. For example, the unfolded radius of $r_2h_3m_6$ in Fig. 1 is eight times greater than the folded radius, while the array height changes from an ideal perfect thinness (no height in the unfolded configuration) to a height as long as twice the folded radius.

Nodes from which there are a greater number of mountain fold creases than valley fold creases are termed mountain nodes. In this research, the mountain nodes of the flasher array are considered to possess acoustic transducer elements like the active nodes labeled with magenta color in

Fig. 1(e), Fig. 1(d), and at the right of Fig. 1(a). It is intuitive that transducers placed on valley nodes would obstruct the conventional folding of the array, hence only mountain folds are activated for the purpose of this research. Patterns formed by mountain nodes shown in Fig. 1(e) are analogous to the spiral or radially acoustic transducer positions in microphone and hydrophone arrays.[15] Although the kinematics of the flasher origami structure are considered in this work along with the rigid interfacing facets, it is noted that the facets are not needed in an implementation of the array so long as all joints are revolute rather than free ball-joint hinges and the shape of the facet is maintained by additional diagonal elements.

Given the concept in this research of acoustic transducers placed on mountain nodes of a reconfigurable flasher-like structure, it is hypothesized that beam patterns with narrow major lobes[15] may be realized by the array when unfolded like that shown in Fig. 1(a). By contrast, once the array is folded into the most compact cylindrical structure observed in Fig. 1(c), the acoustic transducer elements may be nearer than one wavelength, resulting in monopole-like sound radiation and reception.[32] Therefore, a flasher-based reconfigurable acoustic array may exhibit a range of directional and omnidirectional wave guiding

Vivek Srinivas and Ryan L. Harne

properties on the basis of array shape. By folding into a compacted shape the array may benefit applications having severe costs in array transport, such as for underwater towed arrays. This research aims to uncover the opportunities for a flasher-based acoustic array to reconfigure acoustic wave guiding function in ways that may augment conventional DSP of the array transducer element signals. As such, we seek methods to achieve a large variation of wave guiding behavior by physical array shape change. Through the outcomes of this research, DSP application to such physically reconfigurable acoustic arrays may yield versatile and robust tools for airborne and underwater sound localization, acoustic imaging, and other acoustic wave guiding practices.[14,17,32]

This report is organized as follows. Section II introduces the geometric definition of the array nodes and synthesizes this with the Rayleigh's integral to determine wave guiding properties of the array. Section III provides model validation through a proof-of-concept experimental array and data assessment. Section IV investigates the wave guiding capabilities realized by design and implementation of flasher-based acoustic arrays having a broad range of feasible design parameters. Finally, the new findings are summarized with the concluding discussion.

II. MODEL OF A FLASHER-BASED ACOUSTIC ARRAY

This section introduces the kinematic model of the flasher-based acoustic array, the technique to determine the folded configuration, and the method to calculate acoustic wave radiation and reception patterns in the far field from transducers placed on the mountain nodes.

A. Geometric modeling

The kinematic relationships between fully folded and unfolded flasher tessellation crease patterns are defined by Lang et al.[28] and Zirbel et al.[29] and are not summarized here for sake of brevity. Yet, to determine intermediate folded configurations of the tessellation, numerical simulation is required. Hence, in this research, the finite element method technique by Ghassaei et al.[33] is employed to determine the entire kinematic folding sequence of the flasher-based acoustic arrays. The nodal geometry calculated from the simulations is then employed to determine far field sound radiation and reception properties of the array.

B. Acoustic modeling

On the basis of acoustic reciprocity and by considering the far field, this research considers that the acoustic transducers positioned at the mountain nodes of the flasher-based acoustic arrays are either sources or receivers without loss of generality. Hereafter, terminology associated with sound radiation will be used for consistency. In addition, the facets and the crease lines making up the array structure are assumed to be acoustically transparent. If the facets are not employed in practice, then the crease lines and connecting linkages must permit only revolute joint motions to lead to

the correct folding process for the system. Consequently, this research studies the reconfiguration of acoustic transducer elements according to the folding process of the nodes of a flasher origami tessellation.

The Rayleigh's integral for point sources, in other words a Green's function, is used to determine the acoustic field emitted by the array into the far field.[34] A spherical coordinate system is chosen with the origin positioned at the unfolded center point of the respective flasher tessellation, Fig. 2(a). The resulting superposition of all acoustic source contributions to the field point complex acoustic pressure $\mathbf{p}(R, \beta, \theta, t)$ is given by Eq. (1),

$$\mathbf{p}(R, \beta, \theta, t) = j\frac{\rho_o \omega a^2 u_o}{4\pi} e^{j\omega t} \left(\sum_{i=1}^{M} \frac{e^{-jkr_i}}{r_i} \right). \tag{1}$$

Here, r_i is the radial distance between the ith point source and the field point at radial position R respecting the coordinate origin; β is the elevation angle to the field point; θ is the azimuthal angle to the field point; ρ_0 is the density of the fluid medium; ω is the angular frequency of the time-harmonic oscillation of each source; a is the radius of the point source, presumed to be much smaller than the acoustic wavelength; u_0 is the amplitude of the uniform normal velocity of source; M is the number of sources; c_0 is the speed of sound in the fluid medium; and the wavenumber is $k = \omega/c_0$.

The far field axial pressure amplitude is, therefore, a combination of radial and angular influences,

$$p(R, \beta, \theta) = A_{\text{ax}}(R)D(\beta, \theta). \tag{2}$$

The axial pressure amplitude $A_{\text{ax}}(R)$ is given by

$$A_{ax}(R) = \frac{\rho_o \omega a^2 u_o}{R}, \tag{3}$$

while the amplitude of the beam pattern $D(\beta, \theta)$ is given by

$$D(\beta, \theta) = \left| \sum_{i=1}^{M} e^{-jkr_i} \right|. \tag{4}$$

The sound pressure level (SPL) at the field point is computed by Eq. (5),

$$SPL = 20 \log_{10} \left(\frac{p(R, \beta, \theta)}{\sqrt{2}p_{ref}} \right). \tag{5}$$

The reference acoustic pressure is $p_{ref} = 1$ μPa considering an acoustic medium of water and $p_{ref} = 20$ μPa considering airborne acoustic waves.

III. ANALYTICAL MODEL VALIDATION AND ASSESSMENT

To validate the analytical model predictions of far field beam patterns provided by the flasher array, an experimental
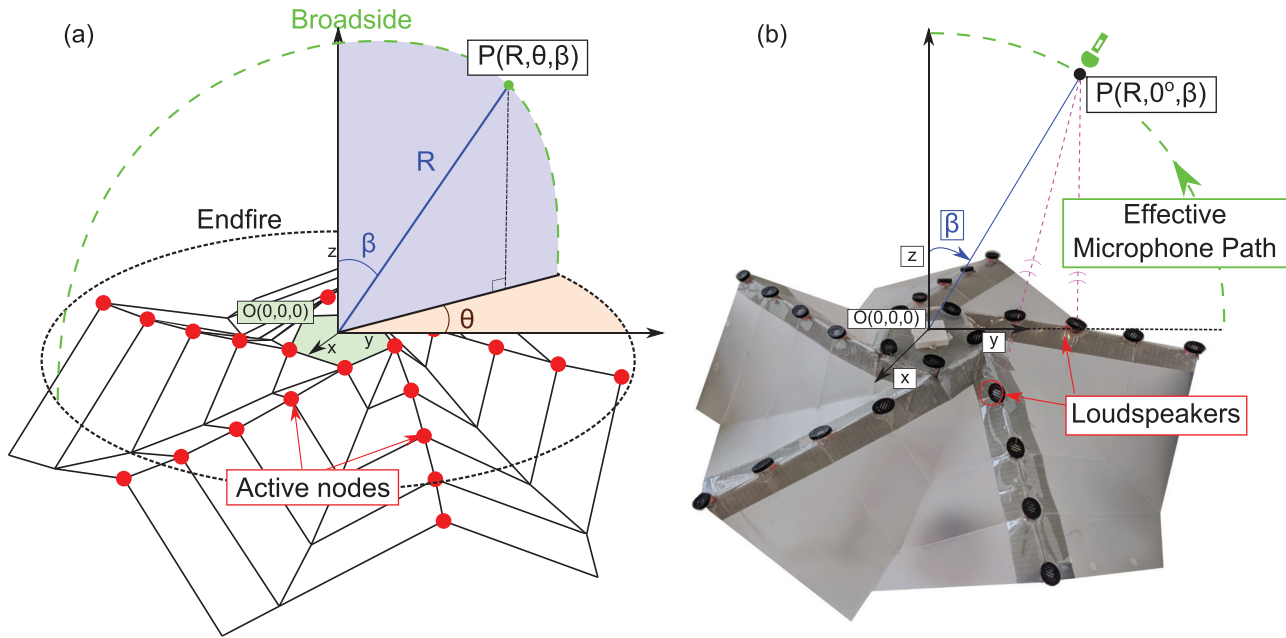
J. Acoust. Soc. Am. **148** (5), November 2020

Vivek Srinivas and Ryan L. Harne   2937

FIG. 2. (Color online) Partially folded flasher array $r_1h_4m_5$. (a) Analytical model and (b) proof-of-concept array geometry.

proof-of-concept array is fabricated and examined in the laboratory. A schematic of the analytical realization and photograph of the experimental array are, respectively, shown in Figs. 2(a) and 2(b). This section describes the experimental sample formulation, experimental protocol, and comparison between model and experimental results.

A. Design and fabrication of proof-of-concept array

A flasher-based acoustic array is fabricated in a crease pattern configuration $r_1h_4m_5$ as shown in Fig. 2. The array has a radius of 30 cm and it is assembled with five sectors $m = 5$. The radius is defined as the radial distance to the outermost node of the array, as shown in Fig. 1(a). Polypropylene sheets of 1.5 mm thickness are scored in the $r_1h_4m_5$ crease pattern using a laser cutter (Epilog Laser Mini 24, Golden, CO). As shown in Fig. 2, the mountain nodes possess acoustic transducers. For the proof-of-concept array, 25 miniature loudspeakers are attached to the mountain nodes via small ball-and-socket joints. Each miniature loudspeaker is a fully enclosed miniature speaker, obviating rear-radiation from the transduction element. The loudspeaker wire terminals are connected by series and parallel interfaces to ensure constant impedance in the speaker network.

B. Experimental methods

Far field measurements of acoustic pressure emitted from the array are taken in air inside a hemi-anechoic acoustic chamber with interior dimensions 7.78, 10.9, and 4.66 m. The proof-of-concept array is mounted to a rigid, rotating stand where the angle of rotation is measured by a rotary encoder. Each miniature loudspeaker is oriented by a ball-and-socket joint to ensure the transducer points normal to the plane of the unfolded array to best emulate the ideal

point source configuration at broadside $\beta = 0°$. A single frequency signal is sent to an audio amplifier (Pyle PFA330, Brooklyn, NY) that drives the array. A microphone (PCB 130E20, Depew, NY) is positioned $R = 3$ m away from the array on a fixed stand. The array is oriented such that the elevation plane at azimuthal angle is $\theta = 0°$ is observed by the microphone. Acoustic pressure is recorded from broadside at elevation angle $\beta = 0°$ to endfire $\beta = 90°$. Acoustic pressure and rotary angle measurements are captured by a data acquisition system (National Instruments USB-6341, Austin, TX) and post-processed using MATLAB to identify the single frequency SPL from the instantaneous frequency spectrum for a given elevation angle.

C. Comparison and discussion

The normal velocity amplitude of the miniature loudspeakers in the array is empirically determined to be $u_0 = 2.5$ mm/s while the radius of the transducer elements is measured and found to be $a = 7.5$ mm. Figure 3 compares the far field beam patterns of the flasher-based acoustic array $r_1h_4m_5$ determined analytically and experimentally. The frequencies considered in the experiments are 1, 2, and 3 kHz, while the percentages of array folding are 0%, 45%, and 80%. Schematics of such folded extents of the array are given at the top of Fig. 3.

Figures 3(b) and 3(c) show that the unfolded flasher acoustic array exhibits confined major lobes at broadside $\beta = 0°$ at the frequencies 2 and 3 kHz. The major lobes constitute the angular regions of high SPL close to broadside before the first local SPL minimum. Such narrow beamwidth corresponds to a constructive/destructive interference combination that would occur specifically at broadside for most acoustic arrays. Yet at 1 kHz in Fig. 3(a), the unfolded state does not lead to a notable major lobe since the
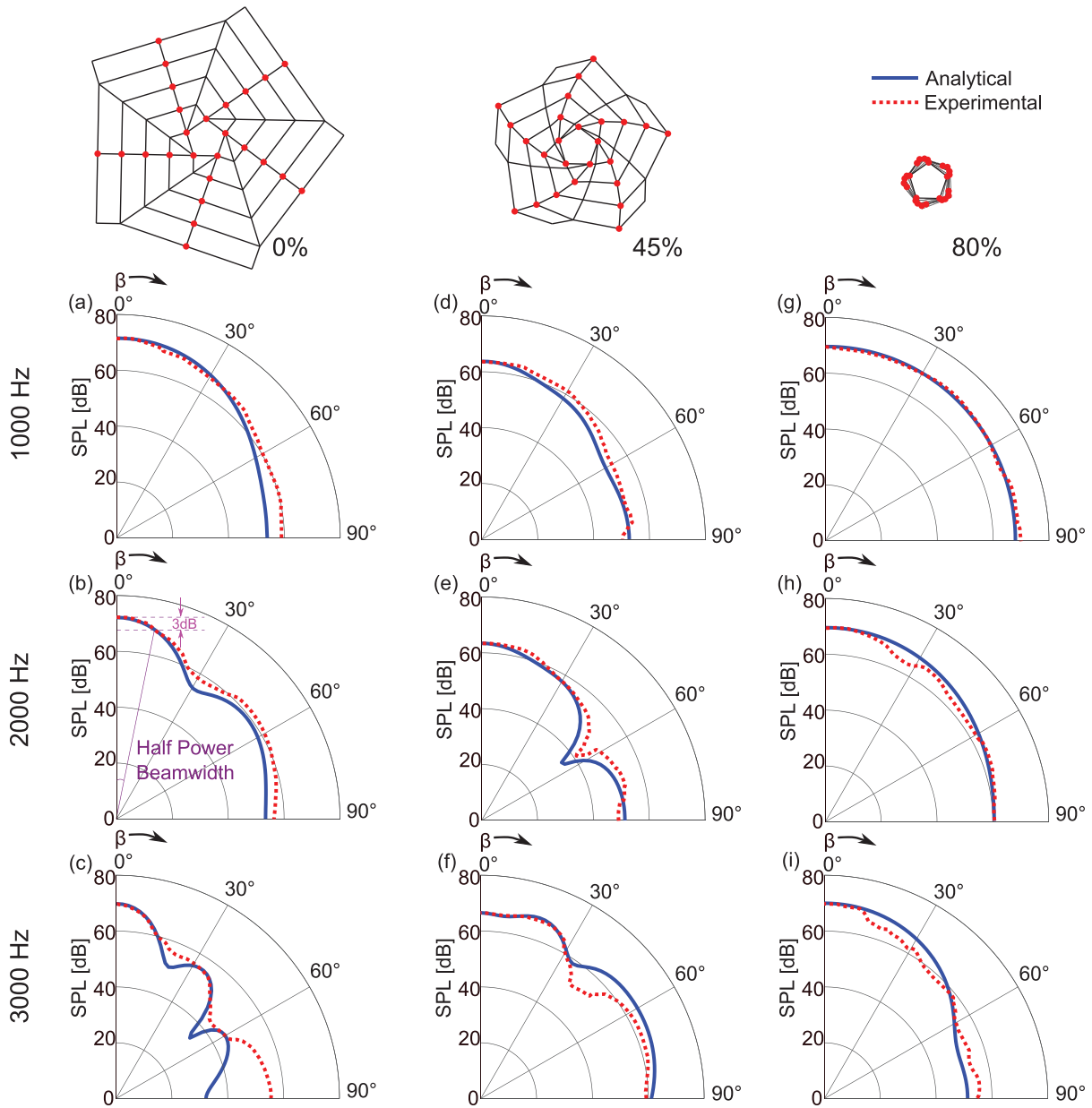
Vivek Srinivas and Ryan L. Harne

FIG. 3. (Color online) Analytical and experimental beam patterns for the $r_1 h_4 m_5$ array in the $y - z$ plane. The SPL is shown for (a) 1000 Hz, 0% folded, (b) 2000 Hz, 0% folded, (c) 3000 Hz, 0% folded, (d) 1000 Hz, 45% folded, (e) 2000 Hz, 45% folded, (f) 3000 Hz, 45% folded, (g) 1000 Hz, 80% folded, (h) 2000 Hz, 80% folded, and (i) 3000 Hz, 80% folded.

wavelength (34.3 cm) is comparable to the radius of the array (30 cm), diminishing potential constructive interference effects.

As the array is folded to 45% and 80% as shown in the center and rightmost columns of Fig. 3, the flasher-based acoustic array leads to more monopole-like sound radiation. This is observed by the uniform SPL across the elevation angle β similar to monopole wave emission. These results give the first conclusive evidence that the flasher acoustic array may transition from a focused wave guide, such as at 3 kHz and unfolded Fig. 3(c), to an effective monopole, such as at 3 kHz and at 80% fold [Fig. 3(i)]. Moreover, the experimental results are in good qualitative and quantitative agreement with the analytical predictions, validating the

analytical model formulation. These results suggest that a flasher-based acoustic array can be realized as a switch between directive and monopole behavior by controlling the array physical reconfiguration.

IV. DETERMINING WAVE GUIDING PROPERTIES OF FLASHER-BASED ACOUSTIC ARRAYS

Shape-adaptive acoustic arrays have myriad of applications in underwater sonar,[35] such as reconfiguring between compacted states for transport to deployed states for long-range communication. DSP techniques may, moreover, be applied in addition to such shape change to tailor acoustic operating functions. In this section, the wave guiding
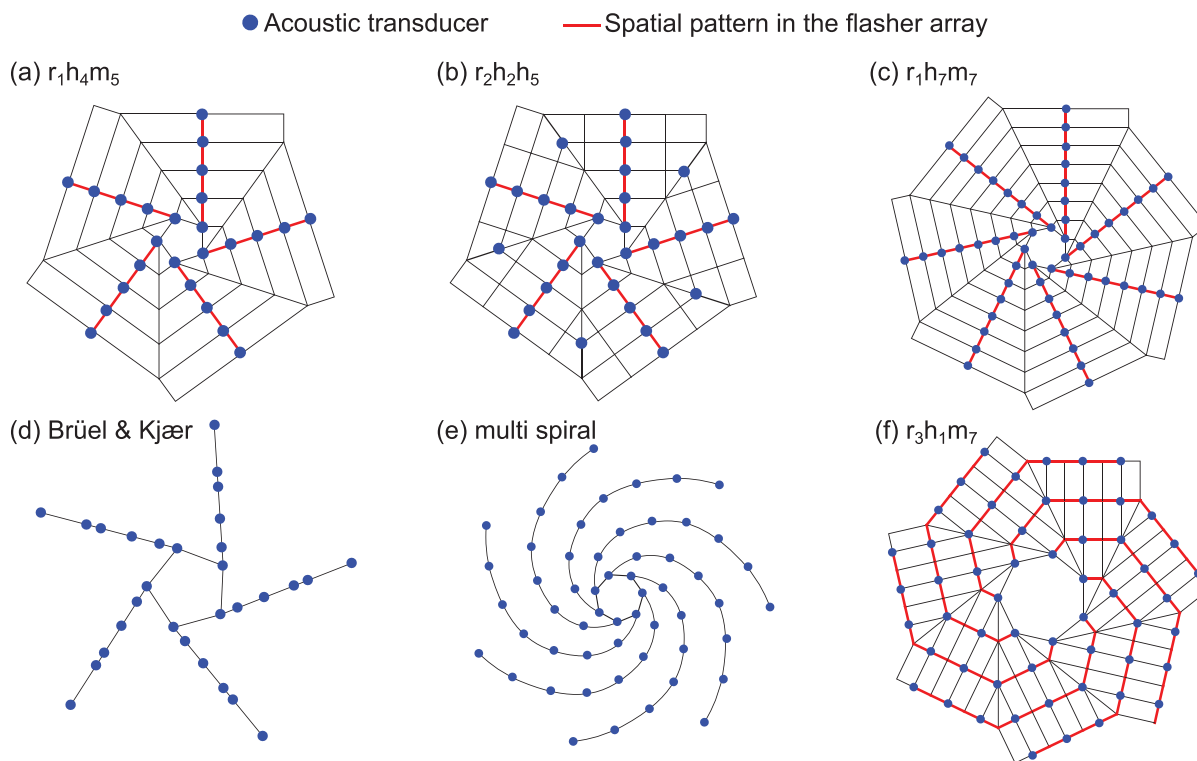
● Acoustic transducer ——— Spatial pattern in the flasher array

(a) $r_1h_4m_5$

(b) $r_2h_2h_5$

(c) $r_1h_7m_7$

(d) Brüel & Kjær

(e) multi spiral

(f) $r_3h_1m_7$

FIG. 4. (Color online) (a) Unfolded $r_1h_4m_5$ flasher-based acoustic array, (b) unfolded $r_2h_2m_5$, (c) unfolded $r_1h_7m_7$, (d) Brüel & Kjær design with straight arm geometry, (e) multi spiral design with spiral arm geometry, and (f) unfolded $r_3h_1m_7$.

properties of the flasher-based acoustic arrays are studied considering water as the fluid medium, seeking insight on the range of acoustic functions achievable by the physically reconfigurable array approach. The flasher arrays examined here use geometries of $r_1h_4m_5$, $r_2h_2m_5$, $r_1h_7m_7$, and $r_3h_1m_7$. The overall array radii are each 50 cm.

The flasher arrays examined in this section are chosen based on similar transducer element locations as those acoustic arrays studied by Prime and Doolan.[15] The folding patterns of the arrays shown in Figs. 4(a), 4(b), 4(c), and 4(f) do not show correct color sequences for the mountain and valley folds and instead highlight by thick red lines the array arms similar to the nominal acoustic arrays studied by Prime and Doolan.[15]

The arrays $r_1h_4m_5$ and $r_1h_7m_7$, shown in Figs. 4(a) and 4(c), have straight arms of transducers similar to the Brüel & Kjær array configuration shown in Fig. 4(d). The nominal multi spiral array shown in Fig. 4(e) has spiral arms originating from the central polygon. The flasher-based acoustic array $r_3h_1m_7$ seen in Fig. 4(f) is designed so as to emulate the multi spiral array configuration. A final flasher acoustic array is studied with the straight radial arm design of $r_2h_2m_5$ to use additional acoustic transducer elements on the second ring as shown in Fig. 4(b).

A. Half power beamwidth for unfolded flasher based acoustic arrays

In Sec. III C it is revealed that the flasher acoustic array exhibits the most directive major lobe in the unfolded state.

Figure 5 presents the half power beamwidth as a function of frequency for the unfolded flasher arrays $r_1h_4m_5$, $r_2h_2m_5$, $r_1h_7m_7$, and $r_3h_1m_7$ as compared to the multi spiral and Brüel & Kjær arrays.[15] The half power beamwidth is defined as the angular width of the radiation pattern that is 3 dB down from the maximum beam level (beam peak), as shown in Fig. 3(b).

Figure 5 reveals that the arrays propagate waves similar to monopoles at low frequency, such as less than around
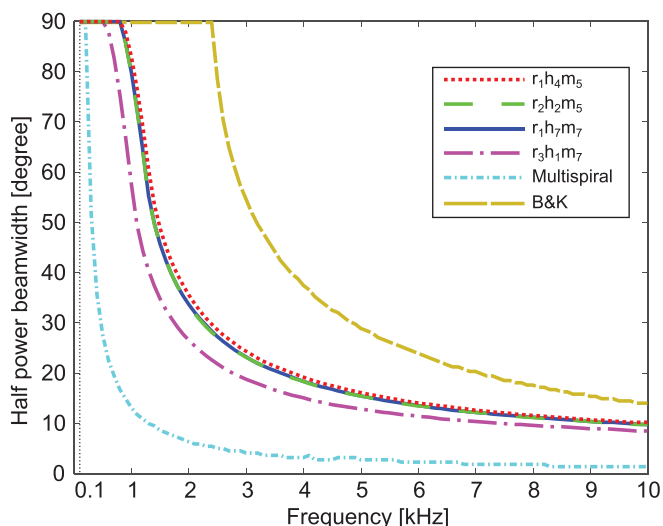

FIG. 5. (Color online) Change in half power beamwidth as a function on frequency for unfolded flashers: $r_1h_4m_5$, $r_2h_2m_5$, $r_1h_7m_7$, $r_3h_1m_7$ multi spiral, and Brüel & Kjær acoustic arrays of radius 50 cm.

Vivek Srinivas and Ryan L. Harne

1 kHz, based on the fact that the half power beamwidth is nearly 90°. In such cases, the wavelength is greater than 50 cm while the array radii are 50 cm, thus prohibiting substantial constructive/destructive interference effects at broadside around the major lobe. With an increase in frequency, the arrays are more directive in the major lobe, leading to narrow angular ranges over which the peak SPL is radiated.

The conventional multi spiral acoustic array exhibits the narrowest beam among all the arrays at all frequencies, seen by the light dot-dashed cyan curve in Fig. 5. The flasher array $r_3h_1m_7$ employs a radial spiral distribution of transducers similar to the conventional multi spiral acoustic array. For the flasher array $r_3h_1m_7$, here the inner radius is 75% of the inner radius of the multispiral array. Furthermore, the curvature on the spirals of the flasher array $r_3h_1m_7$ are inexact recreations of the log spirals on the multispiral array. These discrepancy leads to the slightly different transducer positions. As a result, the half power beamwidths of the flasher $r_3h_1m_7$ is less than multispiral array as seen in Fig. 5. As observed in Fig. 5, the $r_3h_1m_7$ exhibits narrower beams at all frequencies than the arrays with linear transducer configurations: $r_1h_7m_7$, $r_2h_2m_5$, and $r_1h_4m_5$. The flasher arrays with the linear transducer configurations $r_1h_7m_7$, $r_2h_2m_5$, and $r_1h_4m_5$ all have similar values of half power beamwidth, which are less than the half power beamwidth values of Brüel & Kjær array.

Although the flasher arrays $r_1h_4m_5$, $r_2h_2m_5$, and $r_1h_7m_7$ use different numbers of transducers, the arrays exhibit similar changes in half power beamwidth as frequency changes, Fig. 5. On the other hand, while the flasher arrays $r_1h_7m_7$ and $r_3h_1m_7$ utilize the same number of acoustic transducers, the spiral transducer distribution is more directive for $r_3h_1m_7$. Hence, it can be concluded from these results that the placement of transducers is more important than the number of transducers in order to generate a narrower beam pattern at broadside. Specifically, a flasher array with spiral arm transducer distributions results in narrower beams. In addition, Fig. 5 reveals that the unfolded flasher-based arrays exhibit similar trends in directive acoustic wave guiding at broadside as the conventional fixed-shape arrays. Namely, the multi spiral design of the conventional array and of the flasher array $r_3h_1m_7$ provides broadband improvement of underlying beam guiding to broadside than the linear radial distributions of array transducers for the Brüel & Kjær and $r_1h_7m_7$, $r_2h_2m_5$, and $r_1h_4m_5$ arrays.

B. Energy delivered to broadside

Section IV A sheds insight on the angular span of the major lobe only for the unfolded flasher-based acoustic arrays. In this subsection, the relative distributions of acoustic energy to broadside and the endfire regions of the sound field are studied. While broadside and endfire occur for $\beta = 0°$ and $\beta = 90°$, respectively, Fig. 6 highlights the angular regions in which mean values of SPL are determined for broadside and endfire regions. To understand how the
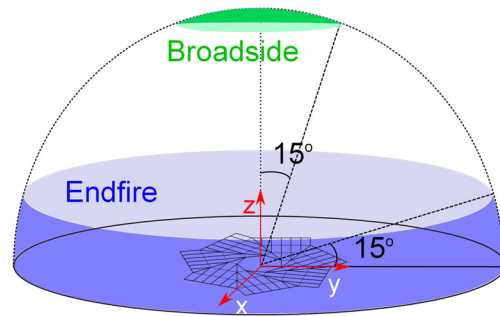

FIG. 6. (Color online) Broadside and endfire regions used to compute mean SPL values.

flasher acoustic arrays change wave guiding properties on the basis of folded configuration, the SPL difference between broadside and endfire regions is calculated as given by Eq. (6). The $\langle x \rangle$ represents the mean of x. The SPL difference quantifies the adaptation of the acoustic field permitted by each flasher array design, helping to shed light on the opportunities afforded by the physical reconfiguration of the origami-inspired arrays,

$$\text{SPL}_{\text{diff}} = \langle \text{SPL}_{\text{Broadside}} \rangle - \langle \text{SPL}_{\text{Endfire}} \rangle. \tag{6}$$

Figure 7 presents the SPL differences defined in Fig. 6 for the flasher arrays $r_1h_4m_5$, $r_2h_2m_5$, $r_1h_7m_7$, and $r_3h_1m_7$ from
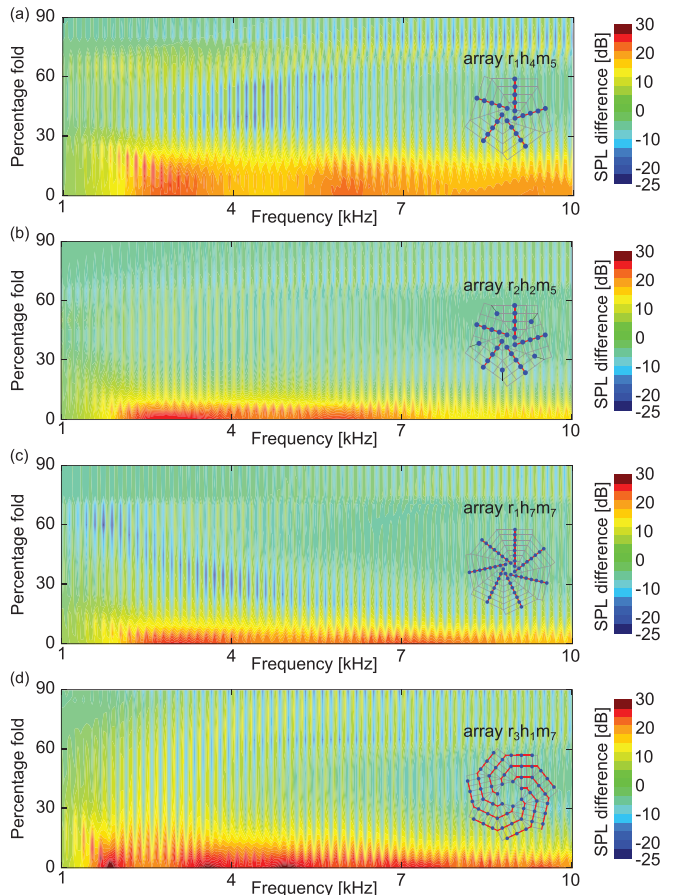

FIG. 7. (Color online) SPL differences for the flasher arrays (a) $r_1h_4m_5$, (b) $r_2h_2m_5$, (c) $r_1h_7m_7$, (d) $r_3h_1m_7$.

J. Acoust. Soc. Am. **148** (5), November 2020

Vivek Srinivas and Ryan L. Harne   2941

1 to 10 kHz and from unfolded (0%) to almost fully folded (90%). Positive values of SPL difference indicate that the beam pattern is directive towards broadside, while negative values of the SPL difference indicate the beam pattern is directive to endfire. The banded nature of the results in the frequency domain in Fig. 7 is a consequence of the difference computation Eq. (6) that uses fixed $15°$ angular increments for broadside and endfire regions. Despite this nuance of the computation, the SPL difference helps to reveal the overall opportunity for sound field adaptation when predefined regions of the acoustic field are of importance.

At the lowest frequencies considered in Fig. 7, each flasher array exhibits monopole-like behavior by way of the SPL difference value near 0 dB. With an increase in frequency, each array exhibits more directive wave guiding, whether towards broadside or endfire. The latter trend holds for arrays folded to small folding percentage since highly folded arrays have little distance between the transducers and thus realize monopole behavior in another form. In other words, for these flasher-based acoustic arrays, monopole-like sound radiation is achieved for low frequencies as well as for highly folded array configurations.

Regardless of array type, for mid to high frequencies such as 4–10 kHz, Fig. 7 shows that the SPL differences are positive valued at small folding percentage and progressively become near-zero valued for greater folding percentage. This indicates that the arrays are directive in unfolded states with large major lobes at broadside, while for highly folded states, the arrays are monopole-like when the acoustic transducers are physically close to together in the highly folded states. These observations are in accordance with findings from Sec. III C.

As observed in Figs. 4(a) and 4(b), the arrays $r_1h_4m_5$ and $r_2h_2m_5$ use the similar transducer distributions excepting that $r_2h_2m_5$ employs five additional transducers on the outer ring. Comparing $r_1h_4m_5$ and $r_2h_2m_5$ in Figs. 7(a) and 7(b), both unfolded arrays exhibit broadside directivity (positive SPL difference), although $r_1h_4m_5$ exhibits such wave guidance over a wider range of fold percentages, i.e., 0%–30% compared to just 0%–10% for $r_2h_2m_5$. Consequently, the additional acoustic transducers in $r_2h_2m_5$ degrade the ability of the array to guide sufficient energy towards broadside. Figures 7(c) and 7(d) show SPL differences for $r_1h_7m_7$ and $r_3h_1m_7$ over the range of percentage fold. The array $r_3h_1m_7$ leads to a much greater SPL difference compared to the array $r_1h_7m_7$. This stands as further evidence that despite using the same number of acoustic transducer elements, the array $r_3h_1m_7$ is more capable of guiding acoustic waves to broadside than $r_1h_7m_7$. As a result, one may conclude that the spiral array geometry of $r_3h_1m_7$ is a more effective, passive wave guiding array geometry than the radial arm distribution of transducers in $r_1h_7m_7$.

C. Sound field generation by flasher-based acoustic arrays

To gather a greater understanding of sound field generation by the flasher arrays, the far field beam patterns at 5 kHz for the arrays $r_1h_4m_5$, $r_2h_2m_5$, $r_1h_7m_7$, and $r_3h_1m_7$ are shown in Fig. 8. Each array exhibits a major lobe at broadside for the unfolded configuration of 0% fold. Yet the radial arm arrays $r_1h_4m_5$, $r_2h_2m_5$, and $r_1h_7m_7$ lead to beam patterns without major side lobes as shown in Figs. 8(a), 8(b), and 8(g). In contrast, the array $r_3h_1m_7$ has a major lobe but a side lobe around $30°$ off of broadside as seen in Fig. 8(h). In fact, this result is confirmed by assessment of Fig. 5 because the smaller half power beamwidth of $r_3h_1m_7$, which is around $15°$ in Fig. 5 at 5 kHz, suggests that the first side lobe occurs for elevation angles near to the beamwidth value. From the standpoint of obtaining effective wave guiding without side lobes, the unfolded arrays $r_1h_4m_5$, $r_2h_2m_5$, and $r_1h_7m_7$ provide better sound projection by virtue of the less energy emitted towards off-axis locations at 5 kHz.

The sound fields created by the arrays when folded to 45% of the compacted state are unique. In fact, for the array $r_1h_7m_7$, there is no major lobe at broadside $\beta = 0°$ in Fig. 8(i). Once fully folded, the array $r_3h_1m_7$ has a side lobe near endfire elevation $\beta = 90°$ and a major lobe at broadside $\beta = 0°$, Fig. 8(l). By contrast, the array $r_1h_7m_7$, which has the same number of transducers as $r_3h_1m_7$, exhibits an omnidirectional beam pattern like a monopole in Fig. 8(k) when fully folded. In other words, the radial arm positioning of the transducers in the reconfigurable flasher arrays may permit guided-to-omnidirectional characteristics such as for the flasher arrays designed according to $r_1h_4m_5$, $r_2h_2m_5$, and $r_1h_7m_7$. On the other hand, the multi spiral type flasher array $r_3h_1m_7$ provides similar functionality yet at lower frequencies, as suggested by Fig. 4 and indicated in Fig. 8 according to higher-order interference phenomena.

V. CONCLUSIONS

This research explores opportunities for a flasher-based acoustic array to reconfigure acoustic wave guiding function in ways that may augment conventional DSP of the array transducer element signals. The origami-inspired acoustic array employs a rotationally symmetric crease pattern with nodal intersections of creases where acoustic transducers are placed. An analytical model is established to define the geometry according to the folded configuration and to predict far field beam patterns based on array operation. Following experimental validation, this research finds that the spatial distribution of the transducers around shared central polygonal geometries is more influential in determining the directive nature of the beam pattern than the number of transducers. For example, a flasher-based acoustic array with spiral arms of transducers exhibits similar beam pattern trends at lower frequencies than flasher arrays with radial arms. On the other hand, because each flasher is a tessellation with radial shape change controlled by folding, all of the arrays studied here exhibit a switching behavior in the beam pattern from broadside directive to omnidirectional. Certain arrays recover broadside directiveness based on the frequency of operation. This research gives inspiration for more versatile digital beamforming implementations of
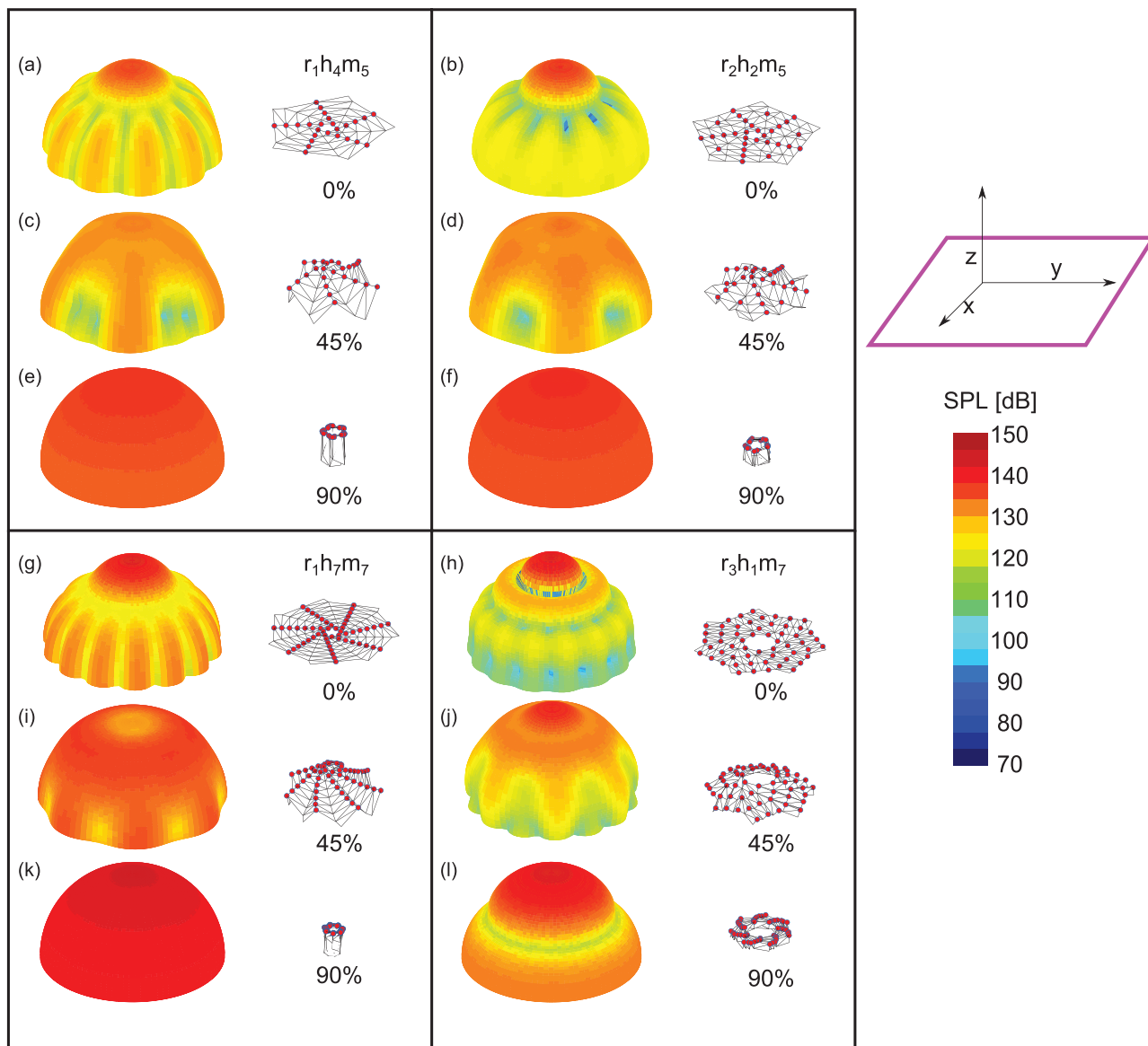
Vivek Srinivas and Ryan L. Harne

FIG. 8. (Color online) SPL beam patterns for the flasher arrays at 5 kHz. The color bars indicate the SPL at the corresponding location in spherical coordinates. (a) $r_1h_4m_5$ 0% folded, (b) $r_2h_2m_5$ 0% folded, (c) $r_1h_4m_5$ 45% folded, (d) $r_2h_2m_5$ 45% folded, (e) $r_1h_4m_5$ 90% folded, (f) $r_2h_2m_5$ 90% folded, (g) $r_1h_7m_7$ 0% folded, (h) $r_3h_1m_7$ 0% folded, (i) $r_1h_7m_7$ 45% folded, (j) $r_3h_1m_7$ 45% folded, (k) $r_1h_7m_7$ 90% folded, and (l) $r_3h_1m_7$ 90% folded.

hydrophone or microphone arrays by reversible physical reconfiguration of transducer elements.

[1] M. R. Bai, J. G. Ih, and J. Benesty, *Acoustic Array Systems: Theory, Implementation, and Application* (Wiley, Singapore, 2013).

[2] C. Zou and R. L. Harne, "Adaptive acoustic energy delivery to near and far fields using foldable, tessellated star transducers," Smart Mater. Struct. **26**, 055021 (2017).

[3] D. H. Johnson and D. E. Dudgeon, *Array Signal Processing: Concepts and Techniques* (Prentice Hall, Englewood Cliffs, NJ, 1993).

[4] J. A. Jensen, H. Holten-Lund, R. Nilsson, M. Hansen, U. Larsen, R. Domsten, B. Tomov, M. Stuart, S. Nikolov, M. Pihl, Y. Du, and J. Rasmussen, "SARUS: A synthetic aperture real-time ultrasound system," IEEE Trans. Ultrason. Ferroelectr. Freq. Control **60**, 1838–1852 (2013).

[5] Z. Li and R. Duraiswami, "A robust and self-reconfigurable design of spherical microphone array for multi-resolution beamforming," in *Proceedings of the IEEE International Conference on Acoustics, Speech, and Signal Processing*, Philadelphia, PA (March 23–25, 2005), pp. 1137–1140.

[6] E. Martinson, T. Apker, and M. Bugajska, "Optimizing a reconfigurable robotic microphone array," in *Proceedings of the 2011 IEEE/RSJ International Conference on Intelligent Robots and Systems*, San Francisco, CA (September 25–30, 2011), pp. 125–130.

[7] D. Theodoropoulos, G. Kuzmanov, and G. Gaydadjiev, "A reconfigurable beamformer for audio applications," in *Proceedings of the 2009 IEEE 7th Symposium on Application Specific Processors*, San Francisco, CA (July 27–28, 2009), pp. 80–87.

[8] H. Luo, K. Wu, R. Ruby, F. Hong, Z. Guo, and L. M. Ni, "Simulation and experimentation platforms for underwater acoustic sensor networks: Advancements and challenges," ACM Comput. Surveys **50**, 28 (2017).

[9] J. V. Thorn, N. O. Booth, and J. C. Lockwood, "Random and partially random acoustic arrays," J. Acoust. Soc. Am. **67**, 1277–1286 (1980).

[10]S. A. Goss, L. A. Frizzell, J. T. Kouzmanoff, J. M. Barich, and J. M. Yang, "Sparse random ultrasound phased array for focal surgery," IEEE Trans. Ultrason. Ferroelectr. Freq. Control **43**, 1111–1121 (1996).

[11]S. Van Doan, T. Cong Tran, and V. Duc Nguyen, "DOA estimation of underwater acoustic signals using non-uniform linear arrays," in *Proceedings of the International Conference on Industrial Networks and Intelligent Systems*, Da Nang, Vietnam (August 27–28, 2018), pp. 103–110.

[12]H. Lee, "Computationally efficient method for estimation of angle of arrival with non-uniform reconfigurable receiver arrays," J. Acoust. Soc. Am. **139**, 1756–1761 (2016).

[13]J. Yu and K. D. Donohue, "Geometry descriptors of irregular microphone arrays related to beamforming performance," EURASIP J. Adv. Signal Process. **2012**, 249.

[14]O. Martínez-Graullera, C. J. Martín, G. Godoy, and L. G. Ullate, "2D array design based on Fermat spiral for ultrasound imaging," Ultrasonics **50**, 280–289 (2010).

[15]Z. Prime and C. Doolan, "A comparison of popular beamforming arrays," in *Proceedings of ACOUSTICS 2013*, Victor Harbor, Australia (November 17–20, 2013), pp. 1–7.

[16]R. Chen, P. Teng, and Y. Yang, "Spiral array design with particle swarm optimization," in *Proceedings of the 2011 IEEE International Conference on Signal Processing, Communications and Computing (ICSPCC)*, Xi'an, China (September 14–16, 2011), pp. 1–4.

[17]A. Price and B. Long, "Fibonacci spiral arranged ultrasound phased array for mid-air haptics," in *Proceedings of the 2018 IEEE International Ultrasonics Symposium (IUS)*, Kobe, Japan (October 22–25, 2018), pp. 1–4.

[18]S. Li, H. Fang, S. Sadeghi, P. Bhovad, and K. W. Wang, "Architected origami materials: How folding creates sophisticated mechanical properties," Adv. Mater. **31**, 1805282 (2019).

[19]S. Babaee, J. T. B. Overvelde, E. R. Chen, V. Tournat, and K. Bertoldi, "Reconfigurable origami-inspired acoustic waveguides," Science Advances **2**, e1601019 (2016).

[20]Y. Zhu, F. Fei, S. Fan, L. Cao, K. Donda, and B. Assouar, "Reconfigurable origami-inspired metamaterials for controllable sound manipulation," Phys. Rev. Appl. **12**, 034029 (2019).

[21]H. Fang, X. Yu, and L. Cheng, "Reconfigurable origami silencers for tunable and programmable sound attenuation," Smart Mater. Struct. **27**, 095007 (2018).

[22]C. Zou, D. T. Lynd, and R. L. Harne, "Acoustic wave guiding by reconfigurable tessellated arrays," Phys. Rev. Appl. **9**, 014009 (2018).

[23]C. Zou and R. L. Harne, "Deployable tessellated transducer array for ultrasound focusing and bio-heat generation in a multilayer environment," Ultrasonics **104**, 106108 (2020).

[24]T. Cambonie and E. Gourdon, "Innovative origami-based solutions for enhanced quarter-wavelength resonators," J. Sound Vib. **434**, 379–403 (2018).

[25]M. Thota, S. Li, and K. W. Wang, "Lattice reconfiguration and phononic band-gap adaptation via origami folding," Phys. Rev. B **95**, 064307 (2017).

[26]M. Thota and K. W. Wang, "Tunable waveguiding in origami phononic structures," J. Sound Vib. **430**, 93–100 (2018).

[27]X. Yu, H. Fang, F. Cui, L. Cheng, and Z. Lu, "Origami-inspired foldable sound barrier designs," J. Sound Vib. **442**, 514–526 (2019).

[28]R. J. Lang, S. Magleby, and L. Howell, "Single degree-of-freedom rigidly foldable cut origami flashers," J. Mech. Robot. **8**, 031005 (2016).

[29]S. A. Zirbel, R. J. Lang, M. W. Thomson, D. A. Sigel, P. E. Walkemeyer, B. P. Trease, S. P. Magleby, and L. L. Howell, "Accommodating thickness in origami-based deployable arrays," J. Mech. Des. **135**, 111005 (2013).

[30]A. J. Taylor, Y. Chen, M. Fok, A. Berman, K. Nilsson, and Z. T. H. Tse, "Cardiovascular catheter with an expandable origami structure," J. Med. Dev. **11**, 034505 (2017).

[31]J. T. Bruton, T. G. Nelson, T. K. Zimmerman, J. D. Fernelius, S. P. Magleby, and L. L. Howell, "Packing and deployable soft origami to and from cylindrical volumes with application to automotive airbags," R. Soc. Open Sci. **3**, 160429 (2016).

[32]E. G. Williams, *Fourier Acoustics: Sound Radiation and Nearfield Acoustical Holography* (Academic Press, San Diego, CA, 1999).

[33]A. Ghassaei, E. D. Demaine, and N. Gershenfeld, "Fast, interactive origami simulation using GPU computation," in *Origami 7*, edited by R. J. Lang, M. Bolitho, and Z. You (Tarquin Publications, Oxford, UK, 2018), pp. 1151–1166.

[34]L. E. Kinsler, A. R. Frey, A. B. Coppens, and J. V. Sanders, *Fundamentals of Acoustics*, 4th ed. (Wiley-VCH, New York, 1999).

[35]R. P. Hodges, *Underwater Acoustics: Analysis*, *Design and Performance of Sonar* (John Wiley & Sons, New York, 2010).